ACS OMEGA

Open Access

http://pubs.acs.org/journal/acsodf

Article

Quasi-One-Dimensional Fibrous Phosphorus: An Air-Stable Low-Symmetry Semiconductor with High Anisotropy

Shuang He, Danmin Liu,* Guoqing Zhang, Feihong Chu, Guoliang Xu, Guoliang Li, Junfeng Liu, Yanhan Yang, and Yongzhe Zhang

Cite This: *ACS Omega* 2024, 9, 43368−43375

Read Online

ACCESS | Metrics & More | Article Recommendations

ABSTRACT: Due to their novel optical and optoelectronic properties, 2D materials have received increasing interest for optoelectronics applications. However, when the width of the channel layer decreases to the nanoscale, the properties of 2D materials can be seriously influenced due to the boundary defects and the approximation of physical dimensions and mean free path of the electron. That brings many challenges to developing novel electronics. Hence, researchers began to maintain their focus on 1D semiconductors without boundary defects and surfaces. Herein, fibrous phosphorus, another Quasi-1D layered semiconducting phosphorus allotrope with air-stable low symmetry, is reported. We found the in-plane anisotropic Raman response and excitation and exciton emission at room temperature. Moreover, the raw materials of fibrous phosphorus are nontoxic and abundant on the earth. These excellent properties will make it a highly competitive material for future applications in the optoelectronic area.

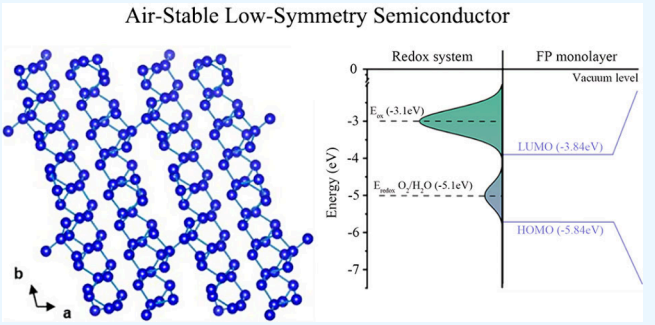

INTRODUCTION

Ever since the discovery of Black phosphorus (BP), there is growing interest in anisotropic 2D materials owing to their unique physical properties and essential electronic and optoelectronic device applications.[1−4] The anisotropy results from the low-symmetry crystal structure. Apart from 2D materials, some 1D materials can achieve large and accessible in-plane anisotropy. Moreover, compared with anisotropic 2D semiconductor materials, 1D materials have no boundary defects or limits of utility in conventional optical systems. In addition, 1D materials may show unusual physical phenomena, including superconductor−insulator transitions,[5] charge density waves,[6] topological insulating properties,[7] electron field emissions,[8] extreme magnetic properties,[9] and Luttinger liquid behavior.[10] However, only a few 1D materials have been investigated so far, such as $TaSe_3$,[11] Sb_2Se_3,[12] coaxial nanotubes,[13] one-dimensional perovskite-like hybrid,[14] and KP_{15}.[15]

Fibrous phosphorus (FP) is another layered semiconducting phosphorus allotrope that was obtained via a chemical vapor deposition (CVD) method from amorphous red P by Ruck et al.[16] Later, Eckstein et al. synthesized FP with $CuCl_2$ as a mineralizing agent.[17] Then, there is no stopping to discover its value. Hu and Roshith et al. found its excellent activity in photocatalysis.[18−21] Lu et al. investigated the structural stability, electronic structures, and optical properties of monolayer FP using DFT calculations.[22] In our research group, Zhang et al. succeeded in obtaining liquid exfoliation processing of 1D FP and then applied it to light cell imaging and fiber devices.[23,24] In fact, researchers seldom pay attention to its low-symmetry structure (triclinic), which may draw in-plane anisotropy to it. As we know, for anisotropic materials, the electrical, optical, thermal, and phonon properties are diverse along with the different in-plane crystal directions. Therefore, the exploration of its anisotropy is of exceptional scientific significance. However, up to now, only Du et al. have studied the giant anisotropic photonics in FP.[25] Research on the anisotropy of FP materials is generally in its early stage.

In this work, we report the stability and anisotropic properties based on experimental research. We investigate the in-plane anisotropic Raman response of layered FP semiconductors through angular-resolved polarized Raman spectroscopy (ARPRS). Furthermore, the angular dependence of excitation and exciton emission was observed in FP by photoluminescence (PL) spectroscopy. These results reveal the intrinsic anisotropy for FP. Such excellent intrinsic anisotropy, in combination with nontoxic and air-stable factors,

Received: March 9, 2024
Revised: July 13, 2024
Accepted: July 18, 2024
Published: October 14, 2024

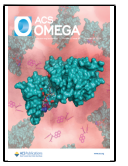

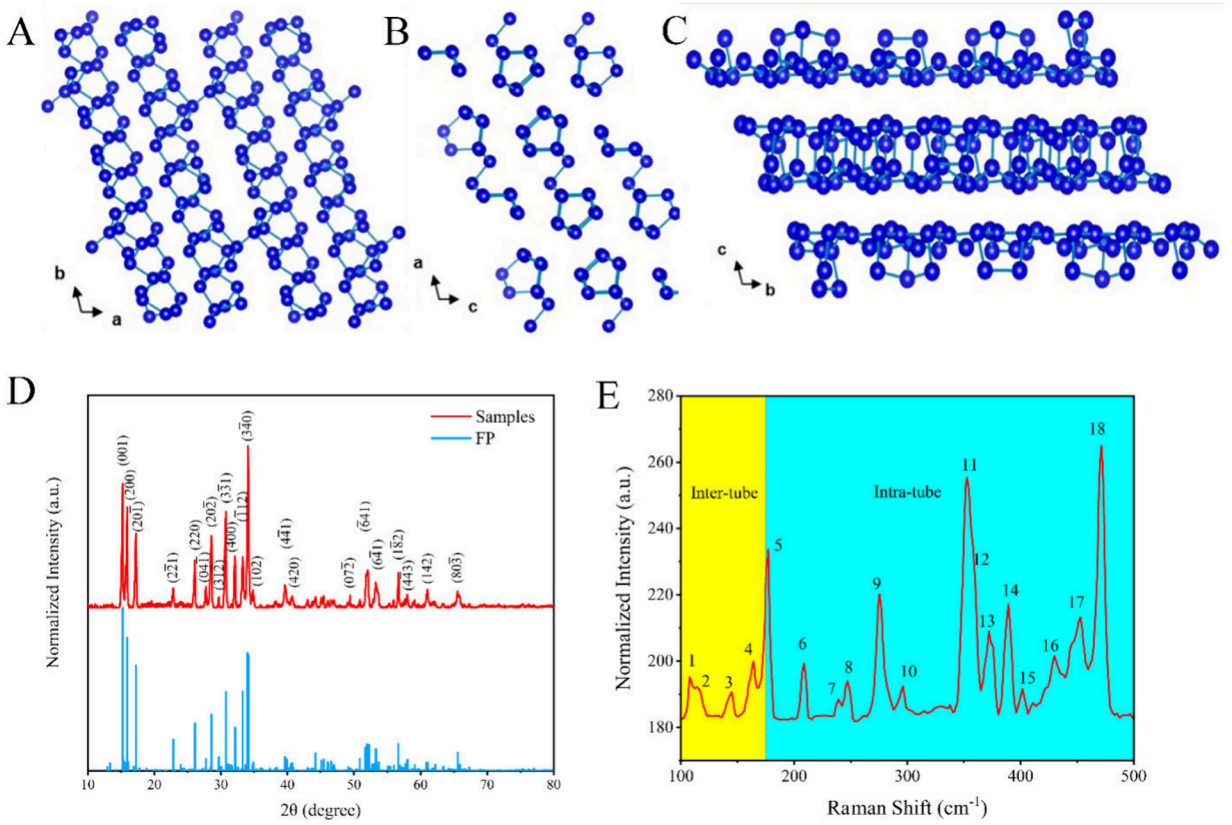

Figure 1. Schematic structural view of the FP crystal along the *a* (A), *b* (B), and *c* (C) directions. (D) The experimentally measured XRD diffractogram and comparison with PDF standard card. (E) Raman result of FP.

makes Q-1D FP a promising candidate for developing electronic and optoelectronic devices in the future.

MATERIALS AND METHODS

Preparation of FP. Fibrous phosphorus was synthesized by loading red phosphorus (99.9999%, 1 g), Sn (40 mg), and SnI_4 (20 mg) into vacuum quartz tubes. The 10 cm vacuum tube was placed in a dual-temperature zone heating system; the temperature gradient was 650 °C/550 °C after heating for 30 min, and after 12 h, the temperature gradually cooled down to 550 °C/450 °C and then cooled down with the furnace. The products were obtained within the walls of the colder end of the glass ampule after breaking the quartz ampule.

Characterization of FP. *XRD.* The powder X-ray diffraction patterns are collected with a Bruker D8 X-ray diffractometer in transmission mode using Cu Kα radiation. The 2θ range is 10−80°, and the scan-step width is 0.02°.

SEM. The SEM image was collected using a FEI Quanta 250 SEM.

TEM. The microstructure of the liquid exfoliated 2D FP was studied by high-resolution transmission electron microscopy (FEI Titan G2).

AFM. A Bruker 8 MultiMode SPM system was used to measure the width and height of mechanically exfoliated FP nanoribbons under the ScanAsyst mode in an ambient environment at room temperature.

Density Functional Theory (DFT). Density functional theory (DFT) simulations were conducted using the Vienna ab initio simulation package (VASP).[26] Element potentials were constructed using the projector augmented wave (PAW) method,[27] and the exchange-correlation component of the density functional was managed through the generalized gradient approximation of Perdew−Burke−Ernzerhof (GGA-PBE) function.[28] For all computations, the energy cutoff for the plane-wave basis was set to 500 eV. Lattice parameters and atomic positions were optimized until the residual forces in each bulk species were less than or equal to 0.001 eV/Å. A vacuum of 30 Å surrounding the sheet was used in all simulations of few-layered configurations. To optimize the system geometry, van der Waals interactions were considered by the Tkatchenko and Scheffler (TS) approach.[29]

Anisotropy Measurement of FP. Raman and PL were used for characterization analysis of anisotropy. The Raman and PL tests were performed by using a WITec Alpha300 confocal Raman microscopy system. The excitation wavelength was 532 nm, and the laser power was kept below 200 μW to avoid sample damage. The polarization of the excitation laser was measured by rotating the fast axis of the half-wave plate positioned in the incident laser path. On the detection side, one polarizer was used to obtain different polarizations of the emission signal.

RESULTS AND DISCUSSION

The crystal structure of bulk fibrous phosphorus (FP) belongs to the triclinic system and the space group $P\bar{1}$ (Figure 1A−C shows its crystal structure). It consists of a "double tube" that is held together by Van der Waals forces in both the a- and c-directions. "Double tube" is formed with the connection of tube and pentagonal phosphorus).

We prepared the bulk crystalline FP by the chemical vapor transport (CVT) method.[24] X-ray diffraction (XRD) was applied to identify the crystal phase of the FP in Figure 1D. All

https://doi.org/10.1021/acsomega.4c02317
ACS Omega 2024, 9, 43368−43375

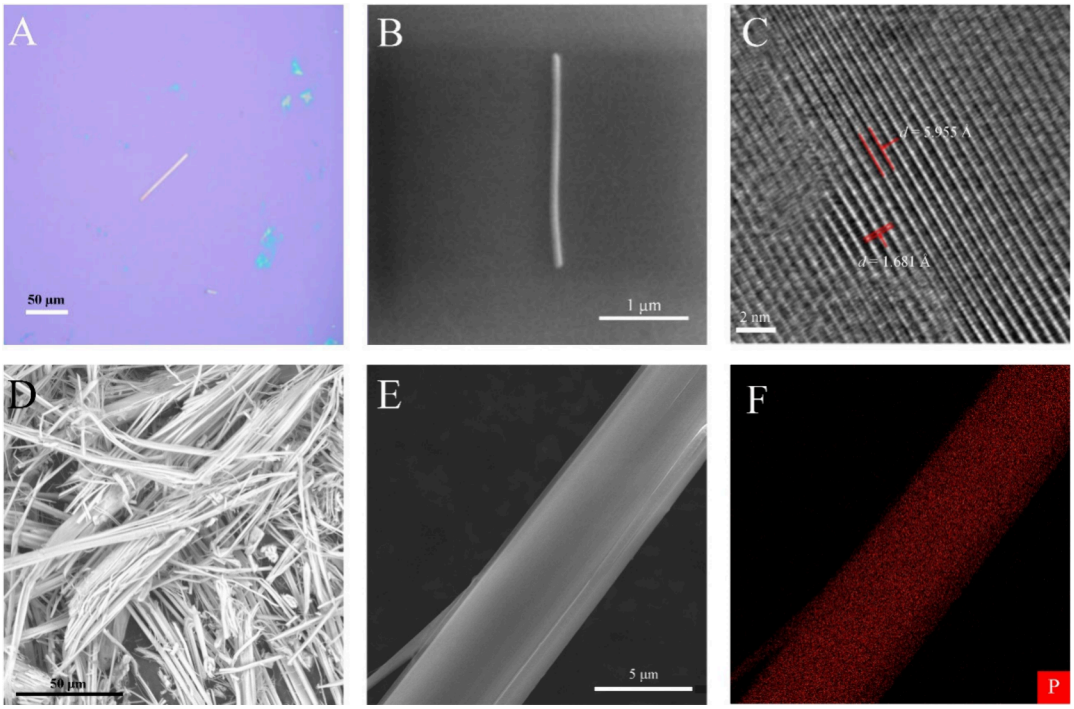

Figure 2. Microstructure of the FP. (A) Light microscope image of a typical FP. (B) Scanning electron microscopy (SEM) image of an FP nanofiber. (C) High-resolution TEM (HRTEM) image of an FP nanofiber. (D) Scanning electron microscope images of block FP. (F) EDS mapping of a single FP (E) under SEM.

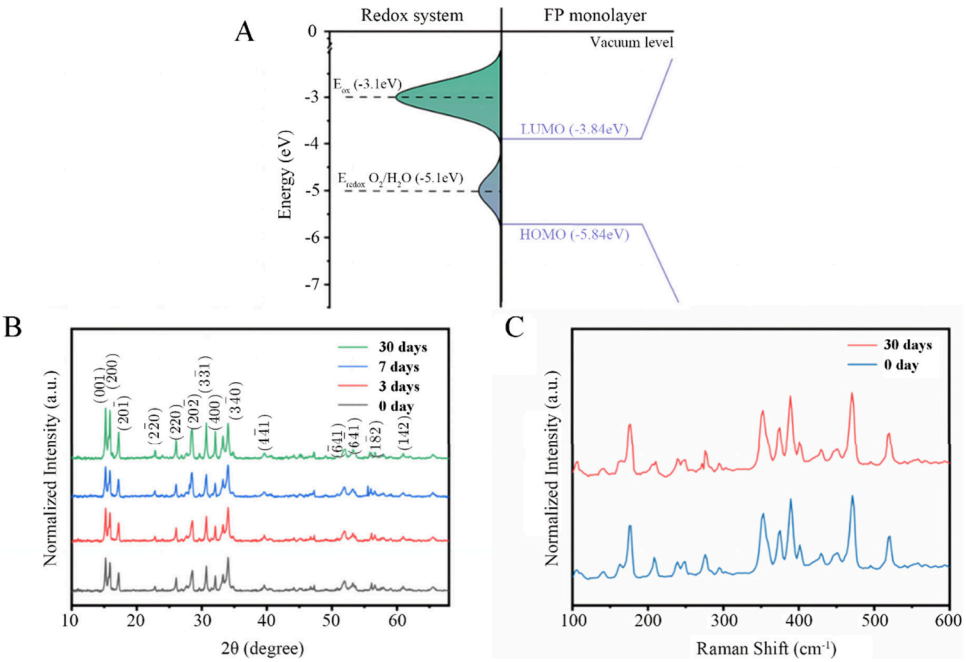

Figure 3. (A) Sketch of the density of states (DOS) for the monolayer FP and the energy diagram of the DOS of the aqueous oxygen acceptor with the solvent reorganization. (B) XRD measurement of FP after exposure in the air experiment. (C) Raman spectra of a typical FP sample were recorded before and after 30 days of air exposure.

diffraction peaks are sharp, directly indicating the well-crystallized formation of FP. As shown in Figure 1E, the locations of the sharp Raman peaks are in agree with the preceding report of FP.[30] This indicates that our samples are indeed FP. The Raman spectral analysis of FP delineates two distinct regions based on vibrational modes. The first region, characterized by intertubular vibrations, encompasses frequencies below 175 cm^{-1}. This region is indicative of the vibrational movements occurring between the tubular structures within the FP. The second region, defined by intratubular vibrations, includes frequencies above 175 cm^{-1}. This latter region reflects the vibrational dynamics occurring within the individual tubular structures of the FP.

https://doi.org/10.1021/acsomega.4c02317
ACS Omega 2024, 9, 43368−43375

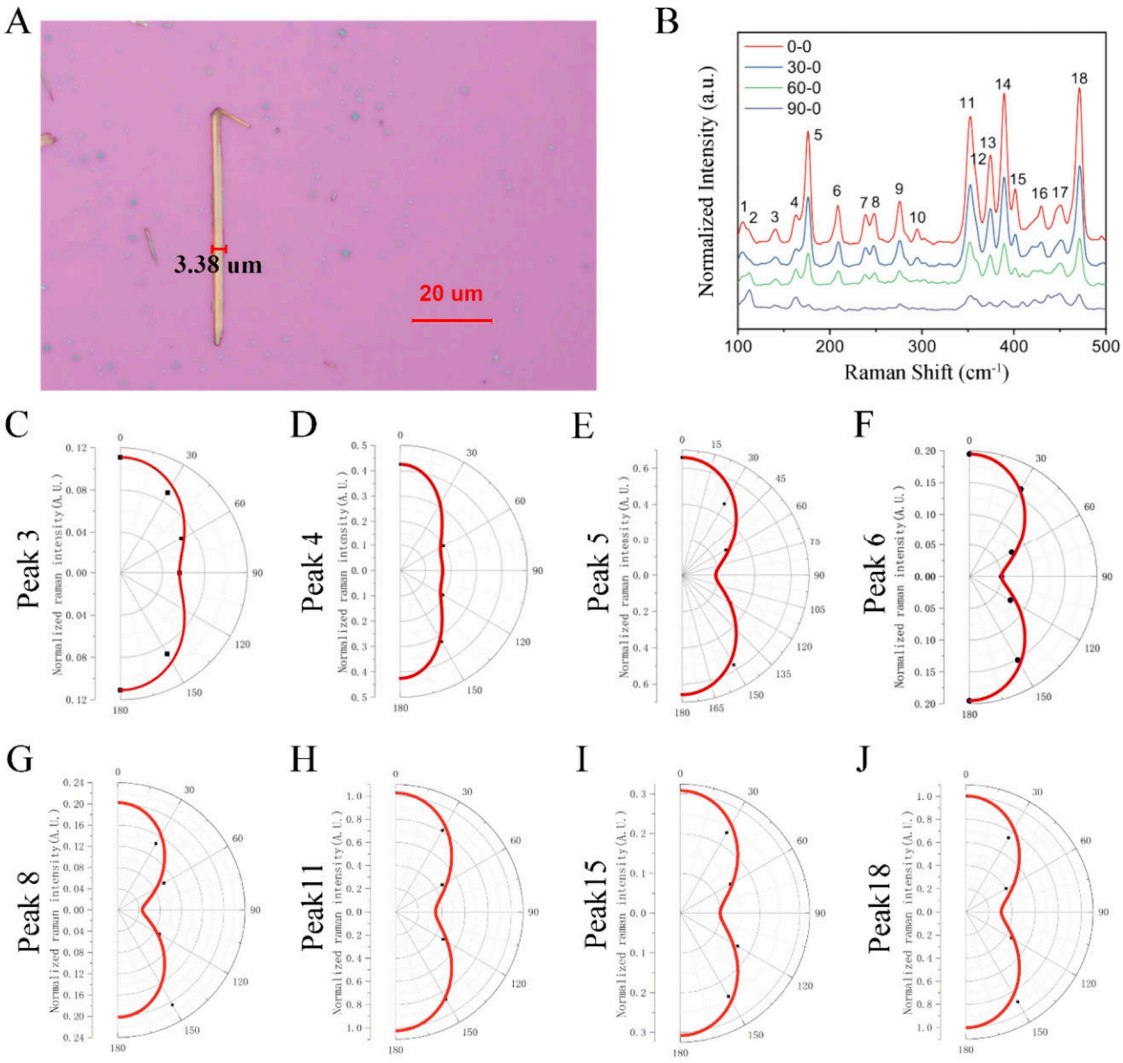

Figure 4. Anisotropic Raman response of FP. (A) The image of the fibrous phosphorus sample; the red line shows the position of the Raman test. (B) Angle-resolved polarized Raman spectra of the FP nanoribbon. (C–J) The intensities of Num.3, Num.4, Num.5, Num.6, Num.8, Num.11, Num.15, and Num.18. Raman peaks of FP as a function of polarization angle θ.

In addition, we observed the morphology of FP. Mechanically exfoliated FP was transferred to a silicon wafer covered with 300 nm SiO_2. The light microscopy and SEM results for a single FP are shown in Figure 2A,B. The FP samples are presented as wires with smooth boundaries. The TEM images provide not only a shape of FP but also its lattice spacing, as shown in Figure 3C. The *d*-spacings of 5.955 and 1.681 Å are visible, corresponding to the $(1\bar{4}1)$ and (301) planes, respectively. From the SEM image of the block FP in Figure 2D, the FP block consists of numerous single FPs, so the FP block can be stripped of the material from the single roots. As the EDS mapping shows in Figure 2E,F, we determined that the sintered samples consisted only of P with a uniform compositional distribution.

The energy levels of dissolved oxygen (O_2(aq)) and its anionic form (O_2^-(aq)) exhibit fluctuations within an approximate range of ±1 eV. Consequently, these levels may coincide with the density of states (DOS) of a monolayer of BP. This overlap facilitates the transfer of electrons from the BP to the solvated oxygen acceptor states, precipitating photoinduced oxidation reactions.[31] In a humid environment, this interaction would result in the degradation of BP. Given that black phosphorene is an allotrope of BP, the question of whether FP can maintain stability under atmospheric conditions remains. To address this, the chemical stability of FP is evaluated using DFT calculations.[32] The calculated band edges of monolayer FP, at −3.84 eV relative to a vacuum, are significantly lower than those of the aqueous O_2 acceptor state, which is at −3.1 eV. This substantial difference hinders carrier transfer between them, thereby rendering the monolayer FP stable under ambient conditions, as depicted in Figure 3A.

Moreover, in order to confirm this, we performed a series of experiments. As Figure 3B shows, the locations of XRD peaks did not change after 3 days, 7 days, and even 30 days. A similar situation can be perceived from the Raman spectrum (Figure 3C). We compare the Raman spectrum of the fresh FP nanotube to that after 30 days of air exposure in ambient conditions. Notably, the profile of all Raman spectra of the FP nanotube displayed only a minor change after 30 days of air exposure, revealing quite outstanding stability in air. This long-term air stability is especially important for practical applications.

Low symmetry of the FP crystal structure indicates that its phonon vibration could be anisotropic. Angle-dependent and

https://doi.org/10.1021/acsomega.4c02317
ACS Omega 2024, 9, 43368−43375

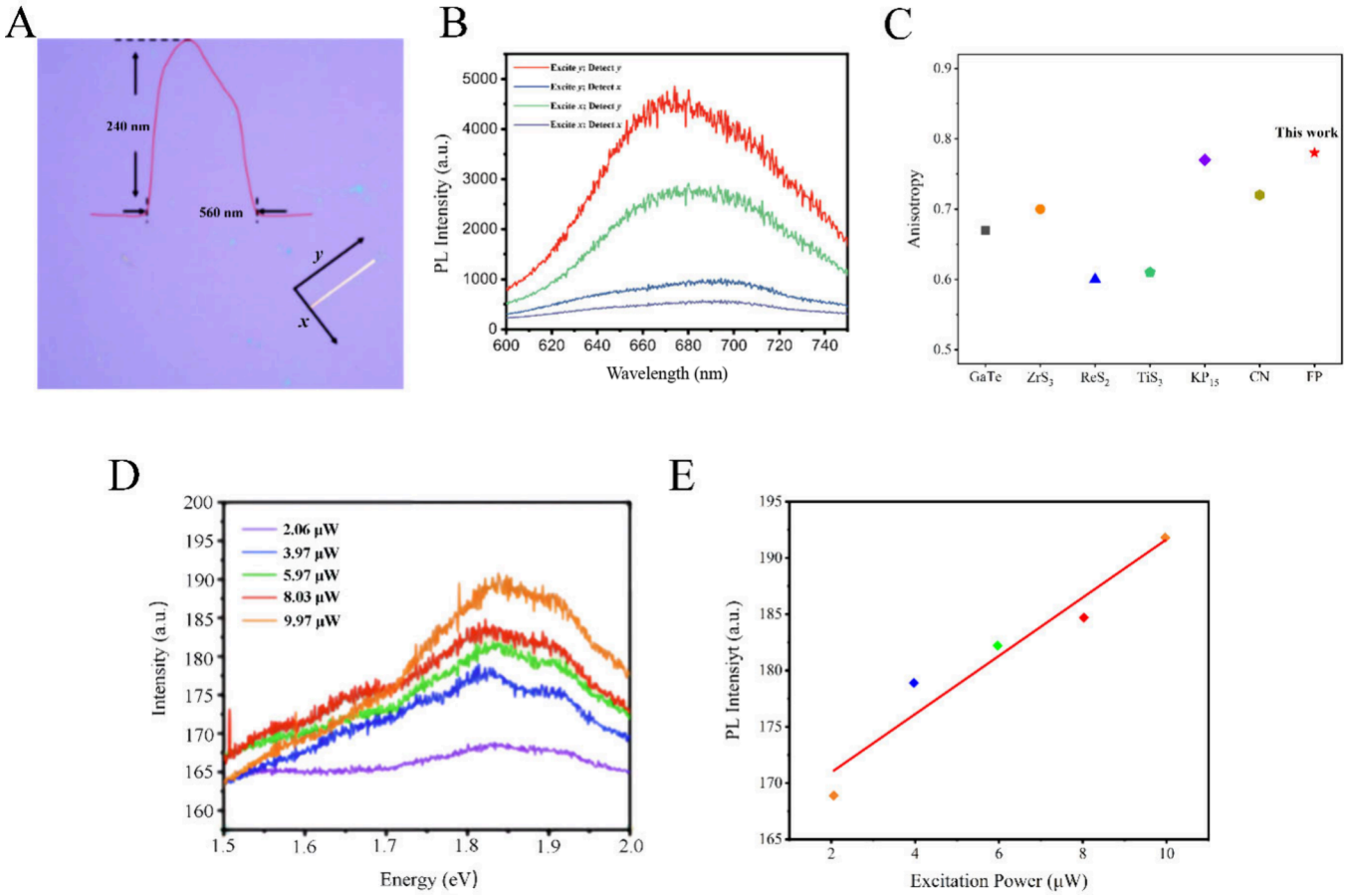

Figure 5. (A) AFM image of the FP. (B) The anisotropic photoluminescence spectrum of the fibrous phosphorus sample. (C) The comparison of anisotropic photoluminescence of FP with GaTe,[38] ZrS_3,[39] ReS_2,[37] TiS_3,[36] KP_{15},[15] and carbon nanotube (CN).[40] (D) Different powers of the photoluminescence spectrum. (E) PL intensity of fibrous phosphorus as a function of excitation laser power.

polarized Raman spectroscopy is a fast, effective, and nondestructive tool that has been widely applied.[33,34] Here, the anisotropic properties of FP are further diagnosed by angular-resolved polarized Raman spectroscopy measurement. The longitudinal direction of the FP nanoribbon was chosen to be along the x-axis of the laboratory coordinate. A half-wave plate positioned in the incident laser path was used to rotate the laser polarization direction. We employed an analyzer set in front of the spectrometer entrance to select the polarization of the Raman signal parallel to the x-axis. We chose the midpoint of the red line of exfoliated FP for examination, as Figure 4A shows. It can be seen in Figure 4B that the relative intensities of all the peaks change significantly with polarization angle θ (the polarization angle between the incident laser and the x-axis). When the laser polarization is parallel to the x-axis, i.e., $\theta = 0°$, the intensities of all the peaks reach the maximum value. On the other hand, when the laser polarization is vertical to the x-axis, i.e., $\theta = 90°$, all the peaks almost disappear. In the context of the sample of nanometers, it has been observed that the Raman scattering intensities for all peaks adhere to a dependence described by the function $\cos^2\theta$ (Figure 4C–J).

The intensity of a Raman active mode is proportional to $\sum_j |e_s R_j e_i|^2$; R_j is the Raman tensor of the crystal structure, e_s and e_i represent the unit polarization vectors of the incident laser and the scattered Raman signal, respectively.[35] The space group associated with FP is denoted as $P\bar{1}$, and its corresponding point group is Ci. Within this framework, there exists a singular type of irreducible representation, for which the associated Raman tensor is designated as $\begin{pmatrix} a & d & e \\ d & b & f \\ e & f & c \end{pmatrix}$. In our angle-resolved polarized Raman configuration, $e_i^T = (\sin\theta, \cos\theta, 0)$, $e_s = (0, 1, 0)$; FP is a layered material with nanoribbons' longitudinal orientation along the [010]. Therefore, the Raman tensor R_j requires conversion to the laboratory's coordinate system R_j' for consistency. It can be expressed by the following equations:

$$R_j' = M \cdot R_j \cdot M^T \tag{1}$$

$$M = \begin{pmatrix} \cos\beta & \sin\beta & 0 \\ -\sin\beta & \cos\beta & 0 \\ 0 & 0 & 1 \end{pmatrix} \tag{2}$$

The angle between the crystal and laboratory coordinates is defined as (β(x = 90−97.91° = −7.91°), where 97.91° is the angle of intersection between the [1 0 0] and [0 1 0] crystallographic directions. Consequently, the Raman intensity for a given Raman mode is denoted as $\{\sin\theta[d\cos^2\beta - d\sin^2\beta + (b-a)\cos\beta\sin\beta]\cos\theta\,[a\cos^2\beta + b\sin^2\beta + 2d\cos\beta\sin\beta]\}^2$. The polarized Raman intensities of all peaks, when analyzed with respect to the angle, can be approximated by the function $\cos^2\theta$. This suggests that the expression of $d\cos^2\beta - d\sin^2\beta + (b-a)\cos\beta\sin\beta$ is nearly zero. Such a result

https://doi.org/10.1021/acsomega.4c02317
ACS Omega 2024, 9, 43368−43375

indicates the inherent anisotropy in the lattice structure of the material KP_{15}. Moreover, the ARPRS measurement can be used to examine the crystalline orientation of FP.

The exfoliated FP exhibits anisotropic characteristics not only in its Raman spectral features but also in its photoluminescence properties. We study the anisotropic photoluminescence properties of FP by PL. In previous research, we found that some samples presented more than one PL peak. This may derive from the total reflection of emitted light that occurs at the interface between the FP block and air as well as the substrate, namely the so-called F−P cavity effect.[24] To avoid the F−P cavity effect, we selected samples with a width of less than 800 nm and a large ratio of length to width. Figure 5A is the AFM image of the FP sample. The results of the polarization-resolved photoluminescence study for a 560 nm wide FP nanoribbon are shown in Figure 5B. The anisotropic photoluminescence spectrum was attained by modifying the direction of incident light polarization and detecting the orientation. When the polarization angle of the laser is fixed, the intensity of the emission peaks observed along the *y*-axis is approximately 4.73 times greater than those observed along the *x*-axis, indicating a pronounced anisotropy in the emission properties. It shows the anisotropic emission property of FP. We also notice the anisotropic excitation, as is seen in Figure 5B. When the detector polarization is kept fixed, the intensity of FP changes dramatically. This trend shows the anisotropic excitation character. As we all know, the PL intensity of materials depends on the following experimental factors, internal quantum efficiency of itself, and their absorptivity to light. Here, we just adjust the polarization of the excitation laser without excitation laser power changes to avoid experimental factor influence on intensity. This indicates that the pronounced anisotropic emission characteristic of FP originates from its highly anisotropic structural composition. To depict the degree of anisotropy, we draw into the polarization ratio. The polarization ratio of FP is 0.78, which is computed by the following formula:

$$\rho = \frac{I_{\parallel} - I_{\perp}}{I_{\parallel} + I_{\perp}} \tag{3}$$

Compare to the other 1D materials (TiS_3,[36] ReS_2,[37] GaTe,[38] KP_{15},[15] ZrS_3,[39] carbon nanotube[40]), FP has a higher polarization ratio (Figure 5C). The large anisotropy indicates its huge potential in photonic and optoelectronic applications.

Furthermore, we also analyzed the source of photoluminescence in FP. As Figure 5D shows, the photoluminescence intensity displays differently under diverse power. According to the former study, if $I \propto P^{\alpha}$ (α is between 1 and 2, I represents the intensity of PL peaks and P represents excitation power), localized states may be the origin of the emission.[41,42] If $I \propto P^{0.5}$, the recombination of localized electron−hole pairs may cause the emission.[43] If $I \propto P^{0.8}$, the emission may stem from excitons bound to defects.[41] Finally, if $I \propto P$, the primary source of emission is the recombination of free excitons.[42,44,45] It is found that there is a linear relationship between the luminescence intensity and excitation power (Figure 5E). Based on this result, we can conclude that the emission of FP is caused by the recombination of the excitons. Additionally, the observation of exciton emission at room temperature implies that FP possesses a high exciton binding energy.

CONCLUSIONS

In summary, we have prepared a quasi-one-dimensional fibrous phosphorus crystal and studied and demonstrated its in-plane anisotropy. Angle-resolved polarization Raman spectroscopy measurements provide strong evidence for the anisotropy of the phonon vibrational modes within the crystal. Photoluminescence measurements similarly observed significant anisotropy in the optical properties of the material. In addition, we have analyzed the origin of the photoluminescence and found larger exciton binding energies. Our work introduces a nontoxic, stable, low-symmetry layered semiconductor. The highly anisotropic optical properties of the material show promise for multifunctional nano- and optoelectronic devices.

AUTHOR INFORMATION

Corresponding Author

Danmin Liu − *Key Laboratory of Advanced Functional Materials, Ministry of Education, College of Materials Science and Engineering, Beijing University of Technology, Beijing 100124, China;* orcid.org/0000-0002-4031-1351; Email: dmliu@bjut.edu.cn

Authors

Shuang He − *Key Laboratory of Advanced Functional Materials, Ministry of Education, College of Materials Science and Engineering, Beijing University of Technology, Beijing 100124, China;* orcid.org/0000-0001-7650-2670

Guoqing Zhang − *Chinese Academy of Sciences Aerospace Information Research Institute, Beijing Institute of Aerospace Standardization, Beijing 100166, China*

Feihong Chu − *Key Laboratory of Advanced Functional Materials, Ministry of Education, College of Materials Science and Engineering, Beijing University of Technology, Beijing 100124, China*

Guoliang Xu − *Key Laboratory of Advanced Functional Materials, Ministry of Education, College of Materials Science and Engineering, Beijing University of Technology, Beijing 100124, China;* orcid.org/0000-0001-5930-6520

Guoliang Li − *Key Laboratory of Advanced Functional Materials, Ministry of Education, College of Materials Science and Engineering, Beijing University of Technology, Beijing 100124, China;* orcid.org/0000-0003-1500-3194

Junfeng Liu − *Key Laboratory of Advanced Functional Materials, Ministry of Education, College of Materials Science and Engineering, Beijing University of Technology, Beijing 100124, China*

Yanhan Yang − *School of Science, Xi'an University of Posts and Telecommunications, Xi'an 710121, China*

Yongzhe Zhang − *Key Laboratory of Optoelectronics Technology, Ministry of Education, Faculty of Information Technology, Beijing University of Technology, Beijing 100124, China;* orcid.org/0000-0002-3471-4402

Complete contact information is available at: https://pubs.acs.org/10.1021/acsomega.4c02317

Author Contributions

He S, Zhang G: Synthesized the fibrous phosphorus materials. He S, Xu G, Li G, Liu J: Characterized the fibrous phosphorus materials. He S, Liu D: Wrote the manuscript. Zhang Y, Yang Y: Provided useful suggestions.

Notes

The authors declare no competing financial interest.

https://doi.org/10.1021/acsomega.4c02317
ACS Omega 2024, 9, 43368−43375

■ ACKNOWLEDGMENTS

The authors would like to acknowledge the financial support of the National Natural Science Foundation of China (NSFC 51972006 and NFSC 52002318).

■ ABBREVIATIONS

BP, Black phosphorus; FP, Fibrous phosphorus; CVD, Chemical vapor deposition; ARPRS, Angular-resolved polarized Raman spectroscopy; PL, Photoluminescence; Q-1D, Quasi-one-dimensional; DFT, Density functional theory

■ REFERENCES

(1) Glavin, N. R.; Rao, R.; Varshney, V.; Bianco, E.; Apte, A.; Roy, A.; Ringe, E.; Ajayan, P. M. Emerging Applications of Elemental 2D Materials. *Adv. Mater.* **2020**, *32* (7), No. 1904302.

(2) Turunen, M.; Brotons-Gisbert, M.; Dai, Y.; Wang, Y.; Scerri, E.; Bonato, C.; Jöns, K. D.; Sun, Z.; Gerardot, B. D. Quantum Photonics with Layered 2D Materials. *Nat. Rev. Phys.* **2022**, *4* (4), 219−236.

(3) Xu, H.; Xu, S.; Xu, X.; Zhuang, J.; Hao, W.; Du, Y. Recent Advances in Two-Dimensional van Der Waals Magnets. *Microstructures* **2022**, *2* (2), No. 2022011.

(4) Ma, Q.; Ren, G.; Xu, K.; Ou, J. Z. Tunable Optical Properties of 2D Materials and Their Applications. *Advanced Optical Materials* **2021**, *9* (2), No. 2001313.

(5) Ning, W.; Yu, H.; Liu, Y.; Han, Y.; Wang, N.; Yang, J.; Du, H.; Zhang, C.; Mao, Z.; Liu, Y.; Tian, M.; Zhang, Y. Superconductor−Insulator Transition in Quasi-One-Dimensional Single-Crystal Nb_2PdS_5 Nanowires. *Nano Lett.* **2015**, *15* (2), 869−875.

(6) Zhang, K.; Liu, X.; Zhang, H.; Deng, K.; Yan, M.; Yao, W.; Zheng, M.; Schwier, E. F.; Shimada, K.; Denlinger, J. D.; Wu, Y.; Duan, W.; Zhou, S. Evidence for a Quasi-One-Dimensional Charge Density Wave in CuTe by Angle-Resolved Photoemission Spectroscopy. *Phys. Rev. Lett.* **2018**, *121* (20), No. 206402.

(7) Huang, H.; Duan, W. Quasi-1D Topological Insulators. *Nat. Mater.* **2016**, *15* (2), 129−130.

(8) Yang, Y. H.; Wang, B.; Xu, N. S.; Yang, G. W. Field Emission of One-Dimensional Micro- and Nanostructures of Zinc Oxide. *Appl. Phys. Lett.* **2006**, *89* (4), No. 043108.

(9) Mihailovic, D.; Jaglicic, Z.; Arcon, D.; Mrzel, A.; Zorko, A.; Remskar, M.; Kabanov, V. V.; Dominko, R.; Gaberscek, M.; Gómez-García, C. J.; Martínez-Agudo, J. M.; Coronado, E. Unusual Magnetic State in Lithium-Doped MoS_2 Nanotubes. *Phys. Rev. Lett.* **2003**, *90* (14), No. 146401.

(10) Chudzinski, P. Parameters of Tomonaga-Luttinger Liquid in a Quasi-One-Dimensional Material with Coulomb Interactions. *Phys. Rev. B* **2021**, *103* (15), No. 155122.

(11) Lin, C.; Ochi, M.; Noguchi, R.; Kuroda, K.; Sakoda, M.; Nomura, A.; Tsubota, M.; Zhang, P.; Bareille, C.; Kurokawa, K.; Arai, Y.; Kawaguchi, K.; Tanaka, H.; Yaji, K.; Harasawa, A.; Hashimoto, M.; Lu, D.; Shin, S.; Arita, R.; Tanda, S.; Kondo, T. Visualization of the Strain-Induced Topological Phase Transition in a Quasi-One-Dimensional Superconductor $TaSe_3$. *Nat. Mater.* **2021**, *20* (8), 1093−1099.

(12) Huang, M.; Xu, P.; Han, D.; Tang, J.; Chen, S. Complicated and Unconventional Defect Properties of the Quasi-One-Dimensional Photovoltaic Semiconductor Sb_2Se_3. *ACS Appl. Mater. Interfaces* **2019**, *11* (17), 15564−15572.

(13) Lin, C.; Qu, L.; Li, J.; Cai, Z.; Liu, H.; He, P.; Xu, X.; Mai, L. Porous Nitrogen-Doped Carbon/MnO Coaxial Nanotubes as an Efficient Sulfur Host for Lithium Sulfur Batteries. *Nano Res.* **2019**, *12* (1), 205−210.

(14) Fan, Q.; Ma, Y.; Xu, H.; Song, Y.; Liu, Y.; Luo, J.; Sun, Z. Near-Room-Temperature Reversible Switching of Quadratic Optical Nonlinearities in a One-Dimensional Perovskite-like Hybrid. *Microstructures* **2022**, *2* (3), 13.

(15) Tian, N.; Yang, Y.; Liu, D.; Liu, X.; Tan, P.-H.; Zhang, D.; Chang, K.; Li, H.; Zhao, M.; Li, J. R.; Tang, X.; Zhang, D.; Zhang, Z.; Xiao, W.; Yan, H.; Zhang, Y. High Anisotropy in Tubular Layered Exfoliated KP_{15}. *ACS Nano* **2018**, *12* (2), 1712−1719.

(16) Ruck, M.; Hoppe, D.; Wahl, B.; Simon, P.; Wang, Y.; Seifert, G. Fibrous Red Phosphorus. *Angew. Chem. Int. Ed* **2005**, *44* (46), 7616−7619.

(17) Eckstein, N.; Hohmann, A.; Weihrich, R.; Nilges, T.; Schmidt, P. Synthesis and Phase Relations of Single-Phase Fibrous Phosphorus. *Zeitschrift anorg allge chemie* **2013**, *639* (15), 2741−2743.

(18) Hu, Z.; Guo, W. Fibrous Phase Red Phosphorene as a New Photocatalyst for Carbon Dioxide Reduction and Hydrogen Evolution. *Small* **2021**, *17* (19), No. 2008004.

(19) Hu, Z.; Yuan, L.; Liu, Z.; Shen, Z.; Yu, J. C. An Elemental Phosphorus Photocatalyst with a Record High Hydrogen Evolution Efficiency. *Angew. Chem. Int. Ed* **2016**, *55* (33), 9580−9585.

(20) Roshith, M.; Kumar, M. S.; Nanda Kumar, A. K.; Ramasubramanian, S.; Stanley, J.; Satheesh Babu, T. G.; Ravi Kumar, D. V. Urchin-like Fibrous Red Phosphorus as an Efficient Photocatalyst for Solar-Light-Driven Disinfection of E. Coli. *J. Photochem. Photobiol., A* **2019**, *384*, No. 112034.

(21) Hu, Z.; Lu, Y.; Liu, M.; Zhang, X.; Cai, J. Crystalline Red Phosphorus for Selective Photocatalytic Reduction of CO_2 into CO. *J. Mater. Chem. A* **2021**, *9* (1), 338−348.

(22) Lu, Y.-L.; Dong, S.; Li, J.; Wu, Y.; Wang, L.; Zhao, H. Fibrous Red Phosphorene: A Promising Two-Dimensional Optoelectronic and Photocatalytic Material with a Desirable Band Gap and High Carrier Mobility. *Phys. Chem. Chem. Phys.* **2020**, *22* (24), 13713−13720.

(23) Zhang, G.; Liu, D.; Tian, N.; Wang, X.; Yan, W.; Huang, Z.; Zhang, Y. Controllable Liquid Exfoliation of Fibrous Phosphorus and Its Live-Cell Imaging. *Inorg. Chem.* **2021**, *60* (7), 4883−4890.

(24) Zhang, G.; Liu, D.; Tian, N.; Liu, B.; Li, S.; You, C.; Qu, X.; Ma, H.; Fan, C.; Zhang, Y. Liquid Exfibration and Optoelectronic Devices of Fibrous Phosphorus. *Inorg. Chem.* **2020**, *59* (2), 976−979.

(25) Du, L.; Zhao, Y.; Wu, L.; Hu, X.; Yao, L.; Wang, Y.; Bai, X.; Dai, Y.; Qiao, J.; Uddin, M. G.; Li, X.; Lahtinen, J.; Bai, X.; Zhang, G.; Ji, W.; Sun, Z. Giant Anisotropic Photonics in the 1D van Der Waals Semiconductor Fibrous Red Phosphorus. *Nat. Commun.* **2021**, *12* (1), 4822.

(26) Kresse, G.; Furthmüller, J. Efficient Iterative Schemes for *Ab Initio* Total-Energy Calculations Using a Plane-Wave Basis Set. *Phys. Rev. B* **1996**, *54* (16), 11169−11186.

(27) Blöchl, P. E. Projector Augmented-Wave Method. *Phys. Rev. B* **1994**, *50* (24), 17953−17979.

(28) Perdew, J. P.; Burke, K.; Ernzerhof, M. Generalized Gradient Approximation Made Simple. *Phys. Rev. Lett.* **1996**, *77* (18), 3865−3868.

(29) Tkatchenko, A.; Scheffler, M. Accurate Molecular Van Der Waals Interactions from Ground-State Electron Density and Free-Atom Reference Data. *Phys. Rev. Lett.* **2009**, *102* (7), No. 073005.

(30) Sun, Z.; Zhang, B.; Zhao, Y.; Khurram, M.; Yan, Q. Synthesis, Exfoliation, and Transport Properties of Quasi-1D van Der Waals Fibrous Red Phosphorus. *Chem. Mater.* **2021**, *33* (15), 6240−6248.

(31) Ignaczak, A.; Schmickler, W.; Bartenschlager, S. Electrochemical Reduction of the O_2 Molecule to the Radical Ion − A Theoretical Approach. *J. Electroanal. Chem.* **2006**, *586* (2), 297−307.

(32) Yang, Y.; Tian, N.; Zhang, Y.; Liu, D.; Zhang, D.; Chang, K.; Yan, H. Rediscovering the MP_{15} Family (M = Li, Na, and K) as an Anisotropic Layered Semiconducting Material. *J. Phys. Chem. Lett.* **2018**, *9* (4), 732−738.

(33) Xia, F.; Wang, H.; Jia, Y. Rediscovering Black Phosphorus as an Anisotropic Layered Material for Optoelectronics and Electronics. *Nat. Commun.* **2014**, *5* (1), 4458.

(34) Wang, Y.; Wu, P.; Wang, Z.; Luo, M.; Zhong, F.; Ge, X.; Zhang, K.; Peng, M.; Ye, Y.; Li, Q.; Ge, H.; Ye, J.; He, T.; Chen, Y.; Xu, T.; Yu, C.; Wang, Y.; Hu, Z.; Zhou, X.; Shan, C.; Long, M.; Wang, P.; Zhou, P.; Hu, W. Air-Stable Low-Symmetry Narrow-Bandgap 2D Sulfide Niobium for Polarization Photodetection. *Adv. Mater.* **2020**, *32* (45), No. 2005037.

https://doi.org/10.1021/acsomega.4c02317
ACS Omega 2024, 9, 43368−43375

(35) Loudon, R. The Raman Effect in Crystals. *Adv. Phys.* **2001**, *50* (7), 813−864.
(36) Khatibi, A.; Godiksen, R. H.; Basuvalingam, S. B.; Pellegrino, D.; Bol, A. A.; Shokri, B.; Curto, A. G. Anisotropic Infrared Light Emission from Quasi-1D Layered TiS_3. *2D Mater.* **2020**, *7* (1), No. 015022.
(37) Wu, S.; Shan, Y.; Guo, J.; Liu, L.; Liu, X.; Zhu, X.; Zhang, J.; Shen, J.; Xiong, S.; Wu, X. Phase-Engineering-Induced Generation and Control of Highly Anisotropic and Robust Excitons in Few-Layer ReS_2. *J. Phys. Chem. Lett.* **2017**, *8* (12), 2719−2724.
(38) Cai, H.; Chen, B.; Wang, G.; Soignard, E.; Khosravi, A.; Manca, M.; Marie, X.; Chang, S. L. Y.; Urbaszek, B.; Tongay, S. Synthesis of Highly Anisotropic Semiconducting GaTe Nanomaterials and Emerging Properties Enabled by Epitaxy. *Adv. Mater.* **2017**, *29* (8), No. 1605551.
(39) Pant, A.; Torun, E.; Chen, B.; Bhat, S.; Fan, X.; Wu, K.; Wright, D. P.; Peeters, F. M.; Soignard, E.; Sahin, H.; Tongay, S. Strong Dichroic Emission in the Pseudo One Dimensional Material ZrS_3. *Nanoscale* **2016**, *8* (36), 16259−16265.
(40) Barkelid, M.; Steele, G. A.; Zwiller, V. Probing Optical Transitions in Individual Carbon Nanotubes Using Polarized Photocurrent Spectroscopy. *Nano Lett.* **2012**, *12* (11), 5649−5653.
(41) Luckert, F.; Yakushev, M. V.; Faugeras, C.; Karotki, A. V.; Mudryi, A. V.; Martin, R. W. Excitation Power and Temperature Dependence of Excitons in $CuInSe_2$. *J. Appl. Phys.* **2012**, *111* (9), No. 093507.
(42) Chiari, A.; Colocci, M.; Fermi, F.; Li, Y.; Querzoli, R.; Vinattieri, A.; Zhuang, W. Temperature Dependence of the Photoluminescence in GaAs-GaAlAs Multiple Quantum Well Structure. *Physica Status Solidi (b)* **1988**, *147* (1), 421−429.
(43) Brener, I.; Olszakier, M.; Cohen, E.; Ehrenfreund, E.; Ron, A.; Pfeiffer, L. Particle Localization and Phonon Sidebands in GaAs/$Al_xGa_{1-x}As$ Multiple Quantum Wells. *Phys. Rev. B* **1992**, *46* (12), 7927−7930.
(44) Huang, J.; Hoang, T. B.; Mikkelsen, M. H. Probing the Origin of Excitonic States in Monolayer WSe_2. *Sci. Rep* **2016**, *6* (1), 22414.
(45) You, Y.; Zhang, X.-X.; Berkelbach, T. C.; Hybertsen, M. S.; Reichman, D. R.; Heinz, T. F. Observation of Biexcitons in Monolayer WSe_2. *Nature Phys.* **2015**, *11* (6), 477−481.

https://doi.org/10.1021/acsomega.4c02317
ACS Omega 2024, 9, 43368−43375